New Journal of Physics
The open access journal at the forefront of physics

Deutsche Physikalische Gesellschaft DPG IOP Institute of Physics

PAPER • OPEN ACCESS

Non-adiabatic quantum state preparation and quantum state transport in chains of Rydberg atoms

To cite this article: Maike Ostmann *et al* 2017 *New J. Phys.* **19** 123015

New Journal of Physics
The open access journal at the forefront of physics

Deutsche Physikalische Gesellschaft DPG
IOP Institute of Physics

Published in partnership with: Deutsche Physikalische Gesellschaft and the Institute of Physics

OPEN ACCESS

RECEIVED
12 July 2017

REVISED
13 October 2017

ACCEPTED FOR PUBLICATION
3 November 2017

PUBLISHED
6 December 2017

PAPER

Non-adiabatic quantum state preparation and quantum state transport in chains of Rydberg atoms

Maike Ostmann[1,2,3], **Jiří Minář**[1,2], **Matteo Marcuzzi**[1,2], **Emanuele Levi**[1,2] **and Igor Lesanovsky**[1,2]

[1] School of Physics and Astronomy, The University of Nottingham, Nottingham, NG7 2RD, United Kingdom
[2] Centre for the Theoretical Physics and Mathematics of Quantum Non-equilibrium Systems, The University of Nottingham, Nottingham, NG7 2RD, United Kingdom
[3] Author to whom any correspondence should be addressed.

E-mail: ppxmo@nottingham.ac.uk

Keywords: quantum information, Rydberg gases, matrix product states, spin chains

Abstract

Motivated by recent progress in the experimental manipulation of cold atoms in optical lattices, we study three different protocols for non-adiabatic quantum state preparation and state transport in chains of Rydberg atoms. The protocols we discuss are based on the blockade mechanism between atoms which, when excited to a Rydberg state, interact through a van der Waals potential, and rely on single-site addressing. Specifically, we discuss protocols for efficient creation of an antiferromagnetic GHZ state, a class of matrix product states including a so-called Rydberg crystal and for the state transport of a single-qubit quantum state between two ends of a chain of atoms. We identify system parameters allowing for the operation of the protocols on timescales shorter than the lifetime of the Rydberg states while yielding high fidelity output states. We discuss the effect of positional disorder on the resulting states and comment on limitations due to other sources of noise such as radiative decay of the Rydberg states. The proposed protocols provide a testbed for benchmarking the performance of quantum information processing platforms based on Rydberg atoms.

1. Introduction

Cold atoms held in optical traps constitute an invaluable tool in the quest for quantum information processing (QIP) and simulation of many-body physics in the quantum regime [1, 2]. Rydberg gases, i.e. atoms excited to high principal quantum number states, are of particular interest as the strong interaction between atoms in the Rydberg states can be exploited for various QIP tasks [3–5]. Experimental progress in manipulating these Rydberg atoms now allows simulating quantum Ising Hamiltonians [6], the adiabatic preparation of the ground states thereof [7], efficient entanglement creation [8] or the implementation of quantum gates [9, 10]. Some of these advances rely on the use of optical tweezer arrays, which permit the creation of various lattice geometries [11] and were recently used to deterministically obtain an optical lattice with close-to-unit filling [12, 13]. Importantly, techniques allowing for addressing a single atom in such arrays have been developed [14–17] opening new possibilities for *non-adiabatic* quantum state engineering, which might help to overcome limitations imposed by the required timescales for adiabatic procedures, where detrimental relaxation effects may become important [18]. First steps in this direction were taken e.g. in [19] which considered optimal control techniques for creation of ferromagnetic GHZ, crystalline or Fock superposition quantum states in Rydberg atoms.

Building on the capabilities of optical tweezer arrays with Rydberg atoms and single site addressing for QIP, we consider GHZ and matrix product state (MPS) engineering and quantum state transport in a one-dimensional geometry. This particular choice is motivated by the fact that all three examples play a fundamental role in QIP and constitute an ideal benchmark in order to assess the performance of the experimental platform we consider—an array of Rydberg atoms—for our theoretical and numerical analysis. Specifically, the GHZ state serves as a reference in quantum estimation theory yielding the Heisenberg scaling [20]. Various proposals exist in the literature for the creation of GHZ states [3, 21, 22] some of which have been realized experimentally,

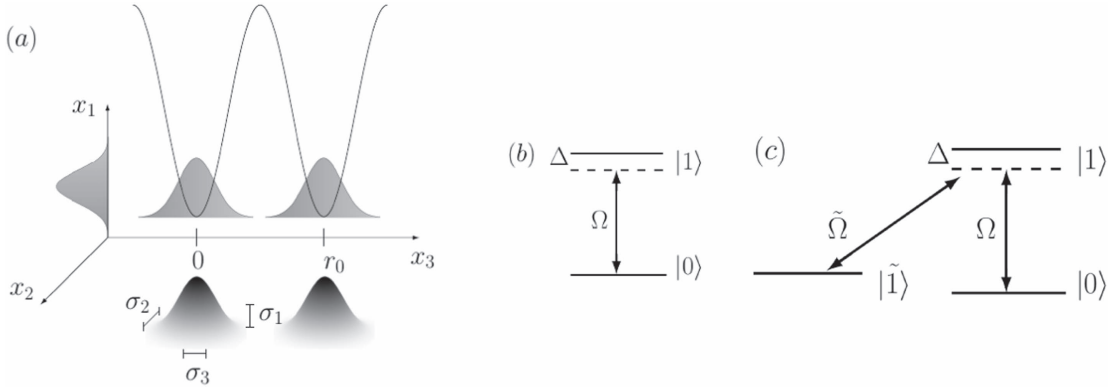

Figure 1. (a) Setup for $N = 2$ atoms. The optical traps are arranged along the x_3 direction and are separated by r_0. The position of the atoms is spread with uncertainty σ_i around their equilibrium values [37]. (b) Level scheme for an effective two level system, where the state $|0\rangle$ is coupled to the Rydberg state $|1\rangle$ by a laser with Rabi frequency Ω. (c) Energy levels of an effective three-level system as it is assumed in the GHZ protocol, where $\tilde{\Omega}$ couples the Rydberg state $|1\rangle$ to another hyperfine state $|\tilde{1}\rangle$.

for example using ultracold ions [23]. Similarly, MPSs play a central role in classical simulations of quantum Hamiltonians in one dimension [24–26] and are naturally realized as ground states of some finite-range interaction spin chains [27–29] which are related to the problem of classical hardcore dimers [30]. For that reason we refer to the class of MPSs considered in this article as dimer-MPS. Importantly, the dimer-MPS feature the so-called Rydberg crystal as a special case [7, 31–33]. Finally, faithful transport of a quantum state between different nodes of a quantum network is an essential requirement for QIP schemes such as quantum computation [34]. Various methods to achieve quantum state transport between spatially separated qubits have been proposed [45–47]. These include schemes based on atoms connected through an optical link [35] or Rydberg atoms, where the transport is achieved through interactions between the Rydberg atoms and atomic ensembles which communicate through a photon exchange [36].

In this paper, the QIP is based on the so-called 'Rydberg blockade' mechanism which relies on the strong repulsive interaction between atoms excited to a Rydberg state [3]. We first introduce the protocols for GHZ state and dimer-MPS generation and quantum state transport in the idealized limit of perfect blockade in section 2. In this regime the blockade mechanism can be effectively described by a three-body Hamiltonian which constitutes the basic building block of the studied protocols. Next, we investigate the influence of more realistic conditions, such as the non-perfect blockade due to the finite value of the interaction energy and the tails of the interaction or the positional disorder of the atoms held in optical tweezers [37] in section 3. There, we relax the requirement of strict blockade and consider instead an evolution guided by a more realistic system Hamiltonian including a van der Waals interatomic potential. This allows us to verify the predictions of the effective description of section 2. To this end we evaluate the fidelity of the produced states with respect to the target as a function of various parameters, such as the Rabi frequency of the laser pulses, interaction strength, length and parity of the chain or the strength of the disorder. We summarize and discuss the results in section 4.

2. Setup, state preparation and state transport protocols

We consider a one-dimensional chain (open boundaries) along the x_3-direction of N optical traps, each occupied with a single atom. A diagram of the setup for the case of two atoms is shown in figure 1(a). The optical traps are separated by equal spacings r_0 so that the position of the kth atom reads $\mathbf{r}_k = (0, 0, kr_0)$. Each atom is described as an effective two level system, where the electronic ground state $|0\rangle$ is coupled to the highly excited Rydberg state $|1\rangle$ via a laser pulse with Rabi frequency Ω as depicted in figure 1(b). For later convenience, we account for the presence of a second hyperfine ground state $|\tilde{1}\rangle$ coupled to the Rydberg state via a second laser with different polarization and Rabi frequency $\tilde{\Omega}$, see figure 1(c).

Considering that the atoms in Rydberg states interact through the van der Waals potential, the Hamiltonian of the system is given by (in the rotating wave approximation)

$$\hat{H} = \sum_{k=1}^{N} \hat{h}_k(\Omega_k, \Delta_k) + \hat{H}_{\text{int}}, \tag{1}$$

where

$$\hat{h}_k(\Omega_k, \Delta_k) = \Omega_k \hat{\sigma}_y^{(k)} + \Delta_k \hat{n}_k \tag{2a}$$

$$\hat{H}_{\rm int} = \frac{V_0}{2} \sum_{\substack{k,m=1 \\ m\neq k}}^{N} \frac{\hat{n}_m\, \hat{n}_k}{|k-m|^6}. \tag{2b}$$

Here, $\hat{\sigma}_y^{(k)} = \mathrm{i}(|1_k\rangle\langle 0_k| - |0_k\rangle\langle 1_k|)$, $\hat{n}_k = |1_k\rangle\langle 1_k|$, the parameter Δ_k is the relative detuning of the laser from the resonant transition between the states $|0_k\rangle$ and $|1_k\rangle$ and $V_0 = C_6/r_0^6$ is the interaction strength proportional to the van der Waals coefficient C_6. Note that in (1) we have allowed for site-dependent Rabi frequencies and detunings Ω_k, Δ_k.

In the regime where $V_0 \gg \Omega_k, \ \forall\, k$, the driving $\propto\Omega_k$, which induces spin flips in the $\hat{\sigma}_z^{(k)}$ basis, cannot overcome the energy cost of having two neighboring Rydberg excitations. This is commonly referred to as the 'Rydberg blockade' mechanism. In this limit, it becomes convenient to adiabatically eliminate blockaded processes: applying a unitary transformation $\hat{U} = \exp[-\mathrm{i}\, t\ V_0 \sum_{k=1}^{N-1} \hat{n}_k \hat{n}_{k+1}]$ on (1), neglecting terms oscillating at the frequencies V_0 and interactions beyond the nearest neighbors and considering resonant excitation $\Delta_k = 0, \ \forall\, k$, one can derive an effective three-body Hamiltonian making the blockade mechanism manifest [27]:

$$\hat{H} = \sum_{k=1}^{N} \hat{h}_k^{\,3\ \rm body}. \tag{3}$$

Here, $\hat{h}_k^{\,3\ \rm body} = \Omega_k\, \hat{P}_{k-1}\hat{\sigma}_y^{(k)}\ \hat{P}_{k+1}$ and $\hat{P}_k = (1 - \hat{n}_k)$ are the projectors on ground-state atoms. The associated unitary evolution corresponding to the application of a laser pulse of duration t_k and area $A_k = \Omega_k t_k$ on the kth atom on the $|l\rangle - |l'\rangle$ transition reads

$$\hat{U}_k^{ll'}(A_k) = \exp(-\mathrm{i}\, t_k\, \hat{h}_k^{\,3\ \rm body}) = \mathbb{1} - \hat{P}_{k-1}\hat{P}_{k+1} + \hat{P}_{k-1}\hat{P}_{k+1}\mathrm{e}^{-\mathrm{i}\, t_k\, \Omega_k\, \hat{\sigma}_y^{(k)}} \tag{4}$$

and represents the basic building block of the protocols studied in this paper[4]. The indices $ll' \in \{01,\ 1\tilde{1}\}$ on the left-hand side of (4) label the basis in which the operators are expressed. For example, $\hat{U}_k^{01}$ means that the operators $\hat{P}_k = 1 - \hat{n}_k$ and $\hat{\sigma}_y^{(k)}$ on the right-hand side of (4) act upon the $\{|0\rangle,\ |1\rangle\}$ basis. We note that for $A_k = \pi$, the unitary (4) corresponds to the Toffoli gate (whose definition we recall in appendix A) with k the target and $k-1,\ k+1$ the control atoms. In what follows we shall refer to the preparation procedure as *non-adiabatic* meaning that the state of the system evolves in a step-wise manner after every application of a gate of the form (4) (or any other local gate) and in general is not an eigenstate of the Hamiltonian of the system, equation (1). This has to be contrasted with adiabatic protocols, where the final state is the ground state of a Hamiltonian whose parameters are adiabatically deformed, starting from an initial ground state that is easy to prepare.

Before we proceed with the introduction of the state preparation and state transport protocols, a comment is in order. The reason for considering the auxiliary hyperfine state $|\tilde{1}\rangle$ is to avoid undesirable effects such as spontaneous emission from atoms in the Rydberg levels or atomic loss and dephasing due to mechanical forces acting on the atoms (van der Waals repulsion [38, 39] and collisions with the background gas). This can be achieved in the three-level scheme when the atomic population is transferred from the Rydberg level $|1\rangle$, after it has been used to implement a particular gate, as fast as possible to the stable hyperfine state $|\tilde{1}\rangle$. However, in order to reduce the complexity of the experiments (which may be important for first proof-of-principle demonstrations) and to further reduce the number of applied gates, we will consider the two-level configuration as well, where only the ground and Rydberg levels $|0\rangle,\ |1\rangle$ are involved. More specifically, we describe the use of both the three and two-level schemes on the example of the GHZ state preparation protocol in section 2.1 and discuss the differences between the two schemes in section 3.1.1. For the reasons mentioned above, we limit the discussion of the dimer-MPS preparation and state transport protocols to the two-level scheme only.

2.1. GHZ state preparation

We consider the non-adiabatic preparation of antiferromagnetic GHZ states of the form

$$|\mathrm{GHZ}\rangle = \frac{1}{\sqrt{2}}(\,|0_1\ \tilde{1}_2\ 0_3\ \ldots\ \tilde{1}_N\rangle + |\tilde{1}_1\ 0_2\ \tilde{1}_3\ \ldots\ 0_N\rangle). \tag{5}$$

They are robust with respect to global noise, such as magnetic or electric field fluctuations on length-scales larger than the length of the chain, as the two components of the state are energetically degenerate: using encoding in the basis $|0\rangle,\ |\tilde{1}\rangle$, this is only strictly true when N is even as one has the same number of excitations (atoms in the state $|\tilde{1}\rangle$) in both components of the GHZ state (the two terms on the rhs of (5)).

Initially all atoms are prepared in the ground state $|\Psi_{\rm in}\rangle = |0\ 0\ 0\ \ldots\ 0\rangle$. First we apply a $\pi/2$-pulse $\hat{U}_1^{01}\left(\frac{\pi}{2}\right)$ on the first atom to generate a superposition state

[4] In principle more general unitaries can be obtained by considering $\hat{h}_k(\mathbf{\Omega}_k,\ \Delta_k) = \Omega_k^x\, \hat{\sigma}_x^{(k)} + \Omega_k^y\, \hat{\sigma}_y^{(k)} + \Delta_k\, \hat{n}_k$.

Table 1. Pulse sequence for the preparation of a GHZ state (left column), the dimer-MPS state (middle column) and the state transport (right column) in a chain of N Rydberg atoms. In the case of the GHZ state, the Rydberg atoms are described as an effective three-level system. However, the GHZ protocol can also be adapted to a two-level description of the atoms by neglecting step (iv). For the dimer-MPS as well as the state transport protocol, each atom is approximated as a two-level system. $|\Psi_{\rm in}\rangle$ is the initial state for the particular protocol.

	GHZ	Dimer-MPS	Transport
$\|\Psi_{\rm in}\rangle$	$\|0\,0\,0\,\ldots\,0\rangle$	$\|0\,0\,0\,\ldots\,0\rangle$	$\|\psi\,0\,0\,\ldots\,0\rangle$
(i)	Apply $\hat{U}_1^{01}\left(\frac{\pi}{2}\right)$	Set counter to $k=1$	Set counter to $k=1$
(ii)	Set counter to $k=1$	Apply pulse of area A_k on atom k (see equations (17))	Apply π-pulse on atom $k+1$
(iii)	Apply $\hat{U}_{k+1}^{01}(\pi)$ if $k=N$ do nothing	$k \Rightarrow k+1$ go back to (ii) till $k=N$ then stop	Apply π-pulse on atom k
(iv)	Apply $\hat{U}_k^{1\tilde{1}}(\pi)$		$k \Rightarrow k+1$ go back to (ii) till $k=N$ then stop
(v)	Move to next atom $k \Rightarrow k+1$ repeat (iii)–(v) till $k=N$		Apply $\mathrm{i}^{N-1}\hat{\sigma}_y^{(N)}$ for N even, see end of section 2.3
# of applied pulses	$2N-1$	N	$2N-2$

$$|\Psi_1\rangle = \hat{U}_1^{01}\left(\frac{\pi}{2}\right)|\Psi_{\rm in}\rangle = \frac{1}{\sqrt{2}}(|0\,0\,0\ \ldots\ 0\rangle + |1\,0\,0\ \ldots\ 0\rangle). \tag{6}$$

This is followed by the application of a π-pulse $\hat{U}_2^{01}(\pi)$ on the second atom

$$|\Psi_2\rangle = \hat{U}_2^{01}(\pi)|\Psi_1\rangle = \frac{1}{\sqrt{2}}(|0\,1\,0\ \ldots\ 0\rangle + |1\,0\,0\ \ldots\ 0\rangle). \tag{7}$$

Note that, due to the blockade mechanism, the second term on the rhs of (6) is not affected by the second pulse. We next go back to the first atom and apply a π-pulse on the $|\tilde{1}\rangle - |1\rangle$ transition in order to transfer any population in its Rydberg level to the hyperfine state $|\tilde{1}\rangle$ so that

$$|\Psi_3\rangle = \hat{U}_1^{1\tilde{1}}(\pi)|\Psi_2\rangle = \frac{1}{\sqrt{2}}(|0\,1\,0\ \ldots\ 0\rangle - |\tilde{1}\,0\,0\ \ldots\ 0\rangle). \tag{8}$$

This is followed by the application of $\hat{U}_3^{01}(\pi)$ on the third atom and $\hat{U}_2^{1\tilde{1}}(\pi)$ on the second atom and so forth until the end of the chain is reached after $2N-1$ gates (unitaries) have been applied. The procedure is summarized in table 1. We note that a similar proposal for the preparation of a ferromagnetic GHZ state was put forward recently in [22].

With the GHZ state preparation protocol just described, the Rydberg state $|1\rangle$ appears neither in the initial nor in the final state, equation (5). It is simply exploited to implement the constrained spin flipping which allows to reconstruct the GHZ pattern in the two components of the state. A simplified two-level version of this protocol, where only levels $|0\rangle$ and $|1\rangle$ are used, is obtained simply by neglecting the transfer from the Rydberg to the hyperfine state, i.e. omitting the step (iv) in table 1.

2.2. Dimer-MPS preparation

It seems natural to explore the effective three-body interaction $\hat{h}_k^{\rm 3body}$ used in the GHZ state preparation for creation of various other quantum states. Specifically, we note that the perfect blockade and the associated Hamiltonian (3) allow in principle for the creation of all possible configurations which are compatible with the dimer-MPS protocol. More precisely, in the blockade regime, simultaneous excitations of adjacent atoms are strongly suppressed, which confines the dynamics to subspaces where the number of neighboring excitations remains constant. In particular, the subspace we work in displays all Rydberg excitations separated by at least one site. In this section we describe how to produce a specific example of such a quantum state which is defined as

$$|z\rangle = \frac{1}{\sqrt{Z_z}}\prod_{k=1}^{N}(\mathbb{1} + z\,\hat{P}_{k-1}\,\hat{\sigma}_k^{+}\,\hat{P}_{k+1})|0\ \ldots\ 0\rangle. \tag{9}$$

Here, z is a real number parametrizing the state, $\hat{P}_k = (1-\hat{n}_k) = |0_k\rangle\langle 0_k|$ is the projector on the atomic ground state introduced after equation (3) and Z_z is an overall normalization constant ensuring $\langle z|z\rangle = 1$. The state (9) is a superposition of all possible configurations without adjacent Rydberg excitations, where each configuration is weighted by z^n with n the total number of (isolated) excitations in it. An illustration of $|z\rangle$ is provided in

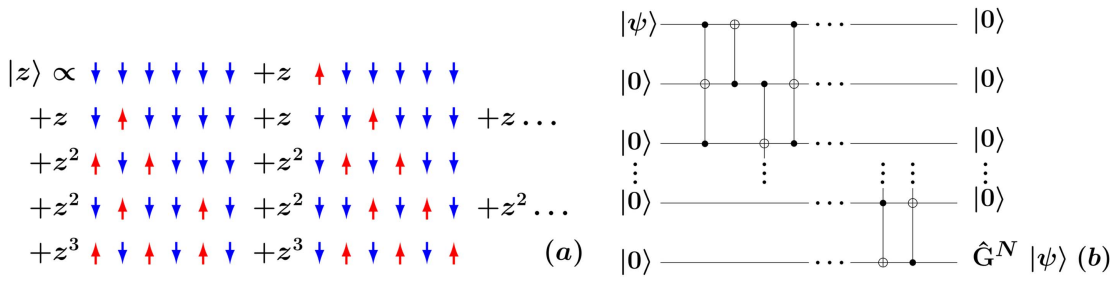

Figure 2. (a) Representation of the dimer-MPS for a chain of $N = 6$ atoms. This state is a superposition of all possible configurations without neighboring Rydberg excitations. The parameter z is weighting the number of excitations in the particular component of the superposition state. (b) Circuit for the transport of a single qubit state $|\psi\rangle$ from the first to the Nth qubit in the chain. All qubits expect the first one, are prepared in the ground state. The CNOT gate as well as the Toffoli gate correspond to a π-pulse with Rabi frequency Ω applied to the particular atom. In the post processing, the $\hat{G}^N$-gate is applied to the state on the Nth qubit, in order to obtain the correct state $|\psi\rangle$.

figure 2(a). Specifically, for $z = 0$, $|z\rangle$ is the product state $|0\ 0\ 0\ \ldots\ 0\rangle$, without any entanglement. For $z = 1$, all possible components are equally weighted, whereas for $z \gg 1$ the ones with higher number of excitations dominate. Note that for odd N and $z \to \infty$, the corresponding dimer-MPS state is a single antiferromagnetic configuration where all odd sites, including the first and the last, have an excited atom. Such an alternating configuration constitutes an example of a so-called Rydberg crystal. However, this state is completely separable and holds no entanglement at all. For the scope of this work, it is therefore convenient to focus on the complementary case: for even N, the major contribution will instead be given by the $N/2 + 1$ configurations with $N/2$ excitations.

It has been shown in [28] that the state (9) admits a matrix product representation

$$|z\rangle = \frac{1}{N} \sum_{i_1,\ \ldots,\ i_N=0,1} [\ \vec{l}\ \hat{X}_{i_1}\ \hat{X}_{i_2}\ \ldots\ \hat{X}_{i_N}\ \vec{r}\ ]\,|i_1\ i_2\ \ldots\ i_N\rangle, \tag{10}$$

with $\hat{X}_0 = (\mathbb{1} - \hat{n}) + z\,\hat{\sigma}_-$, $\hat{X}_1 = \hat{\sigma}_+$ two 2×2 matrices, and ladder operators $\hat{\sigma}_\pm = (\hat{\sigma}_x \pm \mathrm{i}\hat{\sigma}_y)/2$. The vectors $\vec{l} = (z,\ 1)$ and $\vec{r} = (0,\ 1)$ are included to impose the correct boundary conditions.

Furthermore, the same construction leading to (9) can be generalized to the case of a blockade extending over R sites (i.e. an excitation prevents its first R neighbors from being excited) [29]. The analog of the state (9) then reads

$$|z\rangle = \frac{1}{\sqrt{Z_z}} \prod_{k=1}^{N} (\mathbb{1} + z\ \hat{P}_{k,\mathrm{left}}\ \hat{\sigma}_k^+\ \hat{P}_{k,\mathrm{right}})|0\ \ldots\ 0\rangle, \tag{11}$$

where $\hat{P}_{k,\mathrm{left}} = \prod_{j=1}^{R} \hat{P}_{k-j}$, $\hat{P}_{k,\mathrm{right}} = \prod_{j=1}^{R} \hat{P}_{k+j}$ and Z_z is the corresponding normalization constant. This state again admits a MPS representation (10) in which $\hat{X}_0$ and $\hat{X}_1$ are $(R+1) \times (R+1)$ matrices and $\vec{l}$ and $\vec{r}$ $(R+1)$-vectors [29]. As a final remark before describing the state preparation protocol, we would like to mention that the states (9) and (11) are directly related to the ground states of the Hamiltonian (1), see appendix C.2 for details.

In the following, we wish to show that a state of the form (9) (i.e. $R = 1$) can be generated via an appropriate sequence of pulses (see appendix C.1.2 for a more general procedure which applies to generic R). As a first step, we consider how a local pulse of area $A_k = \Omega_k t_k$ acts on a ground state atom located in site k. If the kth atom is blockaded, i.e., if there is an excitation to its left and/or right, then

$$\hat{U}_k^{01}(A_k)|0_k\rangle = |0_k\rangle, \tag{12}$$

whereas if it is not

$$\hat{U}_k^{01}|0_k\rangle(A_k) = \cos A_k|0_k\rangle + \sin A_k|1_k\rangle. \tag{13}$$

The excited component in k will then blockade the following site, so that

$$\begin{aligned}\hat{U}_{k+1}^{01}(A_{k+1})\ \hat{U}_k^{01}(A_k)|0_k 0_{k+1}\rangle = \cos A_k \cos A_{k+1}|0_k\ 0_{k+1}\rangle + \cos A_k \sin A_{k+1}|0_k\ 1_{k+1}\rangle \\ + \sin A_k|1_k\ 0_{k+1}\rangle.\end{aligned} \tag{14}$$

Applying an ordered sequence of local pulses from the first to the last atom $\hat{U} = \prod_{k=N}^{1} \hat{U}_k^{01}$ on the global atomic ground state $|0_1\ \ldots\ 0_N\rangle$ will generically yield components on all elements of the basis in which no neighboring pairs of excitations appear. From equation (13) it is not difficult to see that the component over the initial state will be $C_0 \equiv \prod_{k=N}^{1} \cos A_k$. An excitation in, say, site j will instead come with a $\sin A_j$ and a missing factor

$\cos A_{j+1}$. Using this simple rule, we can work out that the ratio between the component of a generic basis element $C^{(\vec{n})}$ with n (non-neighboring) excitations in $\vec{n} = \{j_1, \ldots j_n\}$ and C_0 will be given by

$$\frac{C^{(\vec{n})}}{C_0} = \prod_{\mu=1}^{n} \left(\frac{\sin A_{j_\mu}}{\cos A_{j_\mu} \cos A_{j_\mu+1}} \right). \tag{15}$$

In order to correctly reproduce state $|z\rangle$, this ratio must be set to be equal to z^n. The only way for this to hold for every possible number n of excitations is to have

$$\frac{\sin A_j}{\cos A_j \cos A_{j+1}} = z \quad \forall\ j. \tag{16}$$

This defines a recursion relation for A_j in terms of A_{j+1}. The natural boundary condition to provide a seed to the recursion is

$$\cos(A_{N+j}) = 1 \quad \forall\ j > 0, \tag{17}$$

which corresponds to requiring that, should the excitation protocol stop before reaching the actual end of the chain, all atoms which have not been addressed should still be in their ground state. Equations (16) and (17) can be analytically solved to yield

$$\cos A_k = \sqrt{2\frac{(1+\sqrt{1+4z^2})^{N+2-k} - (1-\sqrt{1+4z^2})^{N+2-k}}{(1+\sqrt{1+4z^2})^{N+3-k} - (1-\sqrt{1+4z^2})^{N+3-k}}}. \tag{18}$$

Together with the relation $\mathrm{sign}(\sin A_k) = \mathrm{sign}(z)$, the above expressions provide a unique way to extract the pulse areas A_k. Using the values so obtained in the protocol described in table 1 will yield state $|z\rangle$.

2.3. Quantum state transport

In this section we discuss a protocol for the coherent transport of a single qubit state between the two ends of the chain, last column of table 1. We consider a state $|\psi_1\rangle = \alpha|0\rangle + \beta|1\rangle$ to be initialized at the first qubit so that the total initial state reads

$$|\Psi_{\mathrm{in}}\rangle = (\alpha|0\rangle + \beta|1\rangle)_1 \bigotimes |0_2\, 0_3\ \ldots\ 0_N\rangle. \tag{19}$$

The circuit representation of the state transport protocol is shown in figure 2(b). The protocol relies on a sequence of three-body Toffoli gates (see equation (3) and appendix A), which, when applied at the two ends of the chain, becomes effectively a CNOT gate due to the absence of one of the sites. In our implementation, the Toffoli and the CNOT gates flip the target qubit if the controlled qubits are in the ground state $|0\rangle$.

The first step is the application of a π-pulse on the second qubit

$$|\Psi_1\rangle = \hat{U}_2^{01}(\pi)|\Psi_{\mathrm{in}}\rangle = \alpha|0\,1\,0\ \ldots\ 0\rangle + \beta|1\,0\,0\ \ldots\ 0\rangle. \tag{20}$$

As a second step, a π pulse is applied on the first atom

$$|\Psi_2\rangle = \hat{U}_1^{01}(\pi)|\Psi_1\rangle = \alpha|0\,1\,0\ \ldots\ 0\rangle + \beta|0\,0\,0\ \ldots\ 0\rangle, \tag{21}$$

which is then followed by the application of a π-pulse on the third qubit

$$|\Psi_3\rangle = \hat{U}_3^{01}(\pi)|\Psi_2\rangle = \alpha|0\,1\,0\ \ldots\ 0\rangle + \beta|0\,0\,1\ \ldots\ 0\rangle \tag{22}$$

and so on, see the steps (ii)–(iv) in table 1, which are repeated till the end of the chain is reached. At this stage, the initial state $|\psi_1\rangle$ has been successfully transferred so that the state of the Nth qubit reads

$$|\psi_N\rangle = \begin{cases} \mathrm{i}^{N+1}\hat{\sigma}_y|\psi_1\rangle & N \text{ even} \\ |\psi_1\rangle & N \text{ odd}. \end{cases} \tag{23}$$

The presented state transport protocol requires $(2N-2)$ laser pulses and is deterministic as the only required information is the length of the spin chain with no need for a classical communication between the two ends of the chain [40].

3. Imperfections

The above presented protocols for quantum state transport and GHZ and dimer-MPS preparation rely on two important assumptions, namely that the blockade mechanism between two adjacent atoms excited to a Rydberg state is perfect and that the atoms are equally spaced in the chain. Here we analyze in detail the limitations of the protocols when these assumptions are relaxed, namely when the blockade becomes non-perfect due to the finite interaction strength between nearest neighbors and when accounting for interactions beyond nearest neighbors,

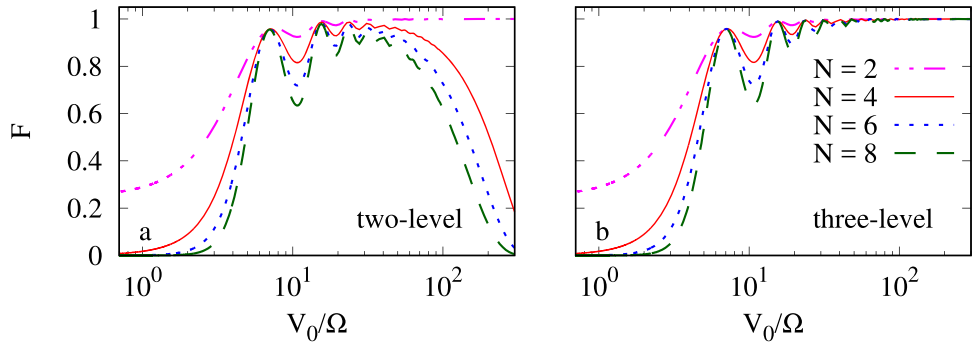

Figure 3. Fidelity of the GHZ state preparation protocol for a two-level description of the atoms (a), as well as the three-level scheme (b) as a function of V_0/Ω. In the three-level implementation of the protocol, atoms are excited to the Rydberg state to effectuate the blockade mechanism and are subsequently transferred to a stable hyperfine state, see text for details. F is given for chains of length $N = 2, 4, 6, 8$, respectively.

and due to the disorder in atomic positions coming from the finite temperature of the atoms and non-vanishing width of the optical traps. In the context of Rydberg gases, the disorder was shown to have a strong impact on the dynamics of spin excitations under the so-called 'anti-blockade' conditions [37]. We comment on other sources of imperfections, such as the influence of relaxation processes, at the end of this section.

3.1. Non-perfect Rydberg blockade

The non-perfect blockade is accounted for by considering the full Hamiltonian (2) featuring van der Waals interaction between all the atoms excited to a Rydberg state. In this case, when a pulse of area $A_k = \Omega_k\, t_k$ is applied to the kth atom, the idealized unitary gate (4) becomes

$$\hat{W}_k^{01}(A_k = \Omega_k\, t_k) = \exp(-\mathrm{i}\, t_k(\hat{h}_k(\Omega_k,\, \Delta_k = 0) + \hat{H}_{\mathrm{int}})). \tag{24}$$

In what follows, considering the full Hamiltonian (2) amounts simply to replacing the unitary gates $\hat{U} \to \hat{W}$ in table 1, which are operators acting on the full Hilbert space of dimension 2^N. The non-perfect blockade results in configurations with adjacent Rydberg excitations. This limits the fidelity of the produced states defined as

$$F \equiv \langle \Psi_{\mathrm{target}}|\ \rho_{\mathrm{final}} |\Psi_{\mathrm{target}}\rangle, \tag{25}$$

where ρ_{final} is the state at the output of the particular protocol described in table 1 and $|\Psi_{\mathrm{target}}\rangle$ is the desired target state. We note that $\rho_{\mathrm{final}} = |\Psi_{\mathrm{final}}\rangle\langle\Psi_{\mathrm{final}}|$ is pure by construction for the GHZ and dimer-MPS protocol as it is defined on all atoms of the chain; on the other hand, it is generally mixed for the transport protocol as we trace over all but the last qubit. In what follows we consider the Rabi frequency Ω to be identical for all atoms. We also neglect the effect of the decay of the Rydberg states, which we justify in section 3.3.

3.1.1. GHZ state preparation

We start our analysis by examining the influence of the non-perfect Rydberg blockade on the GHZ state preparation described in the first column of table 1 with the replacement $\hat{U}^{01} \to \hat{W}^{01}$ and where $|\Psi_{\mathrm{target}}\rangle = |\mathrm{GHZ}_N\rangle$ (we recall that here N is even). The effect of the finite interaction strength can be seen in figure 3, where we plot the fidelity (25) versus the ratio of the nearest-neighbor interactions strength and the Rabi frequency V_0/Ω. Figure 3(a) shows a situation when using the two-level scheme. Figure 3(b) then shows the fidelity in the three-level scheme, where the atoms are transferred from the Rydberg state $|1\rangle$ to the hyperfine state $|\tilde{1}\rangle$.

It is apparent from figure 3 that in the limit $V_0/\Omega \to 0$, i.e. in the absence of the blockade, the fidelity goes to zero in all cases (except $N = 2$ in the three-level scenario, where it is straightforward to show that $F \to 1/4$). In the opposite limit of the infinite blockade $V_0/\Omega \to \infty$, the vanishing of the fidelity in the two-level scenario can be easily understood as the blockade length extends over the whole chain allowing thus only for a single Rydberg excitation to be present. In contrast, in the three-level scenario there is never more than one atom in the Rydberg level at any given time, which results in unit fidelity in that limit.

For intermediate values of V_0/Ω, one can observe oscillations of the fidelity F. The origin of those oscillations can be understood on the example of two atoms (see the magenta line in figure 3). Here the final state is obtained after application of one pulse at each atom and reads

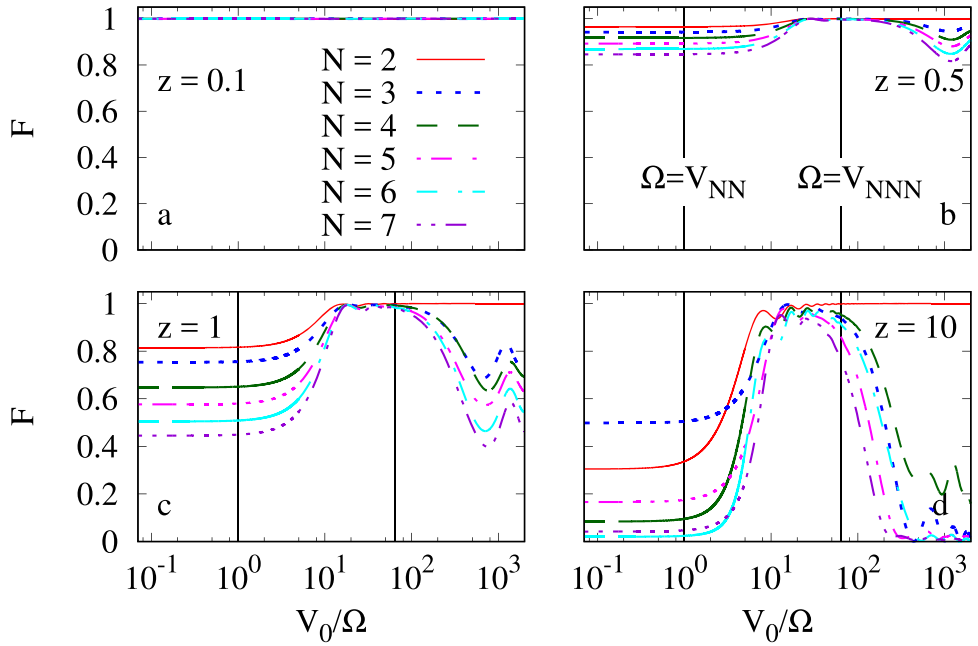

Figure 4. Fidelity of the dimer-MPS preparation protocol for $N = 2$ up to $N = 7$ atoms as a function of V_0/Ω and for $z = 0.1, 0.5, 1, 10$ (a)–(d). See text for details.

$$|\Psi_{\text{final}}\rangle = \hat{W}_2^{01}(\pi)\,\hat{W}_1^{01}\left(\frac{\pi}{2}\right)|00\rangle = \frac{1}{\sqrt{2}}(|0\,1\rangle + \gamma|1\,0\rangle + \delta|1\,1\rangle), \tag{26}$$

where

$$\gamma = \mathrm{e}^{-\mathrm{i}\frac{\pi V_0}{8\Omega}}\left(\cos\left(\pi\frac{\tau}{8\Omega}\right) + \frac{\mathrm{i}V_0\sin\left(\frac{\pi\tau}{8\Omega}\right)}{\tau}\right), \tag{27a}$$

$$|\delta| = \sqrt{1 - |\gamma|^2}, \tag{27b}$$

$$\tau = \sqrt{V_0^2 + 16\Omega^2}. \tag{27c}$$

The term $\delta\ |1\ 1\rangle$ in (26) occurs due to the finiteness of the interaction strength V_0, and reduces the fidelity of the produced state (25), which reads

$$F_{N=2} = \frac{1}{4}\,|1 + \gamma|^2. \tag{28}$$

While there are quantitative differences in the fidelity curves depending on the number of the atoms, we have verified that, for the atom numbers considered, the position of the maxima of the oscillations change only very slightly and thus the expressions (27) provide accurate estimates (which become exact for $N = 2$) for the values of V_0/Ω which maximize the fidelity.

3.1.2. Dimer-MPS preparation

In analogy to the GHZ case, we investigate the effect of the non-perfect Rydberg blockade on the fidelity of the state obtained by applying the protocol described in the second column of table 1, where $|\Psi_{\text{final}}\rangle = |z\rangle$, equation (10), and using again the replacement $\hat{U}^{01} \to \hat{W}^{01}$. Figure 4 shows the influence of the non-perfect Rydberg blockade on the dimer-MPS state preparation protocol on the example of $z = 0.1, 0.5, 1, 10$, for $N = 2$ to $N = 7$ atoms in a chain, respectively. For $z = 0.1$ (figure 4(a)), the fidelity is approximately unity over the whole parameter range. This is a consequence of the fact that for $z \ll 1$, the dominant term in the state (10) is the vacuum (all atoms in the ground state $|0\rangle$) which is not affected by the blockade mechanism.

When increasing z, terms containing more and more atoms in the Rydberg state $|1\rangle$ are becoming relevant with the limiting situation $z \gg 1$, where the dimer-MPS is dominated by terms containing $N/2$ $[(N+1)/2]$ excitations for N even [odd]. Similarly to the GHZ case, the drop of fidelity for small (large) V_0/Ω is due to non-perfect blockade (blockade extending beyond nearest neighbor).

We indicate by vertical lines in figures 4(b)–(d) the values of $\Omega = V_{\text{NN}} = V_0$ and $\Omega = V_{\text{NNN}}$ corresponding to the interaction energies of nearest and next-to-nearest excitations respectively. The optimal fidelity can be expected to be found within the region delimited by these two boundaries. In fact, for $\Omega \gg V_{\text{NN}}$

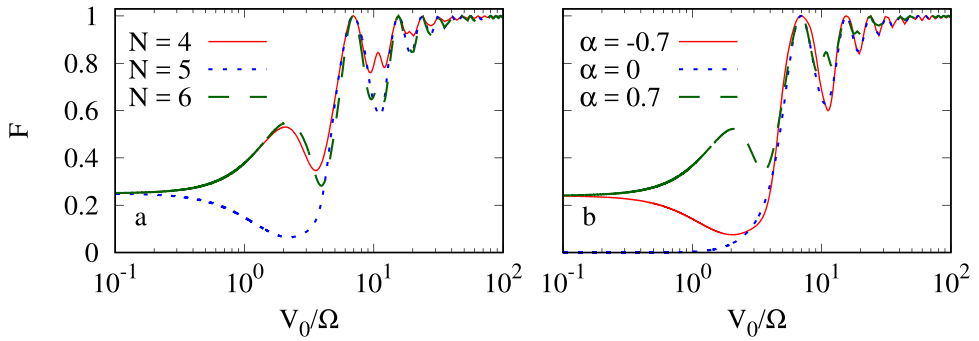

Figure 5. (a) Fidelity of a coherent transport process for $N = 4, 5, 6$ as a function of V_0/Ω. The transferred state is $|\psi_1\rangle = 1/\sqrt{2}\ (|0\rangle + |1\rangle)$. (b) Comparison of the fidelity of the transport process for different initial states $|\psi_1\rangle$ for $N = 4$. The parameter α ($\beta = \sqrt{1-\alpha^2}$) of the state $|\psi_1\rangle = \alpha|0\rangle + \beta|1\rangle$ is varied.

the blockade is relaxed and pairs of neighboring excitations are frequently produced. Conversely, for $\Omega \ll V_{\mathrm{NNN}}$ the next-to-nearest neighbor interaction (partially) blockades atoms two lattice sites away from an excitation, again spoiling the state preparation procedures described above.

3.1.3. Quantum state transport

Using the notation from section 2.3, the target state is the state of the first atom to be transferred, $|\Psi_{\mathrm{target}}\rangle = |\psi_1\rangle$, while the final (single-qubit) state $\rho_{\mathrm{final}} = \mathrm{Tr}_{\neq N}(|\psi_t\rangle\langle\psi_t|)$ is obtained by tracing out all but the Nth atom and $|\psi_t\rangle$ is the target state obtained using the transport protocol with $\hat{U}^{01} \to \hat{W}^{01}$. Figure 5(a) shows the fidelity of the transport process for an initial state $|\psi_1\rangle = 1/\sqrt{2}\ (|0\rangle + |1\rangle)$ at the first atom, for $N = 4, 5, 6$. The decrease in the fidelity and the oscillations in the small and large V_0/Ω limit have the same origin as in the case of dimer-MPS and GHZ state preparation, namely a vanishing blockade for $V_0/\Omega \to 0$ and imperfect blockade due to the finiteness of V_0 respectively.

Next, in order to demonstrate the influence of the initial state on the resulting fidelity, in figure 5(b) we plot the fidelity versus V_0/Ω for $|\psi_1\rangle = \alpha\ |0\rangle + \beta\ |1\rangle$, $\beta = \sqrt{1-|\alpha|^2}$, for $\alpha = -0.7,\ 0,\ 0.7$. It can be seen that in the parameter regime of interest ($V_0/\Omega \gtrsim 5$), the fidelity is independent of α with the maxima coinciding for the α considered. As in the GHZ case, the nature of the observed oscillations can be exemplified on the elementary example of two atoms for which we get

$$\hat{W}_1^{01}(\pi)\hat{W}_2^{01}(\pi)|\Psi_1\rangle = \alpha(\gamma|0\ 1\rangle + \gamma'|1\ 1\rangle) + \beta(\delta|0\ 0\rangle + \delta'|1\ 1\rangle + \delta''|0\ 1\rangle),$$

where $\gamma,\ \delta$ are given by (27) and

$$|\gamma'| = \sqrt{1-|\gamma|^2}, \tag{29a}$$

$$\delta' = \frac{2\mathrm{e}^{-\frac{\mathrm{i}\pi V_0}{4\Omega}}\Omega\left(-\mathrm{i}V_0 + \mathrm{i}V_0\cos\left(\frac{\pi\tau}{4\Omega}\right) + \tau\sin\left(\frac{\pi\tau}{4\Omega}\right)\right)}{\tau^2}, \tag{29b}$$

$$\delta'' = \sqrt{1-|\delta|^2-|\delta'|^2}. \tag{29c}$$

In the case of a perfect Rydberg blockade, only the terms $\alpha\gamma|0\ 1\rangle$ and $\beta\delta|0\ 0\rangle$ would occur after the application of the two laser pulses.

3.2. Non-perfect blockade and position disorder

In lattice systems the atomic positions are typically considered to be fixed. In realistic experiments however, there is a finite uncertainty in their positions due to their finite temperature and finite extent of the optical traps realizing the lattice sites. This can have dramatic consequences e.g. on the excitation transport in the chains of Rydberg atoms [37]. Based on our previous work [37] we here recall the notions needed for the study of the effect of disorder on the protocol's performance.

The position disorder stems from the fluctuations of the atomic positions $\mathbf{r}_k = \mathbf{r}_k^{(0)} + \delta\mathbf{r}_k$ and consequently of the interaction energies (2b). Here, $\delta\mathbf{r}_k$ are drawn from a three-dimensional Gaussian distribution

$$p_{\mathrm{pos}}(\mathbf{r}^{(k)}) = \frac{1}{(2\pi)^{2/3}\sigma_1\sigma_2\sigma_3}\exp\left[-\frac{(\delta r_1^{(k)})^2}{2\sigma_1^2} - \frac{(\delta r_2^{(k)})^2}{2\sigma_2^2} - \frac{(\delta r_3^{(k)} - kr_0)^2}{2\sigma_3^2}\right] \tag{30}$$

with widths σ_i, $i = 1, 2, 3$ in the three spatial directions, see figure 1(a), where $\sigma_i = \sqrt{k_B T/(m\omega_i^2)}$ is given by the temperature T and the mass m of the atoms and the trap frequencies ω_i (see [37] for details).

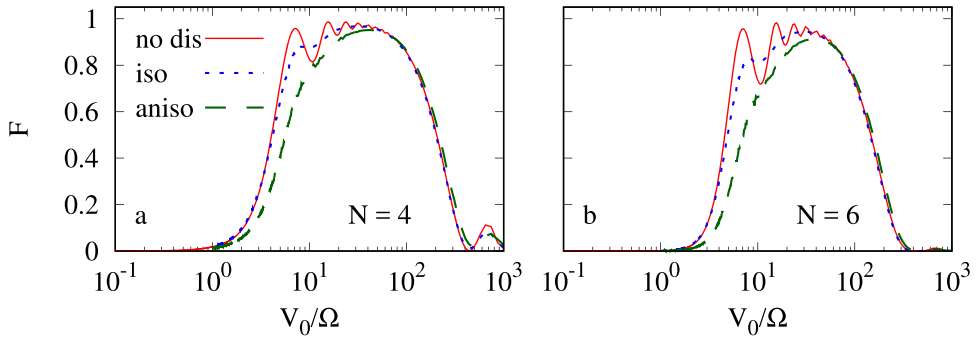

Figure 6. Fidelity of the GHZ state preparation protocol including the effect of non-perfect blockade and disorder for $N = 4$ (a) and $N = 6$ (b) atoms as a function of V_0/Ω with no (solid red), isotropic (dotted blue) and anisotropic (dashed green) disorder.

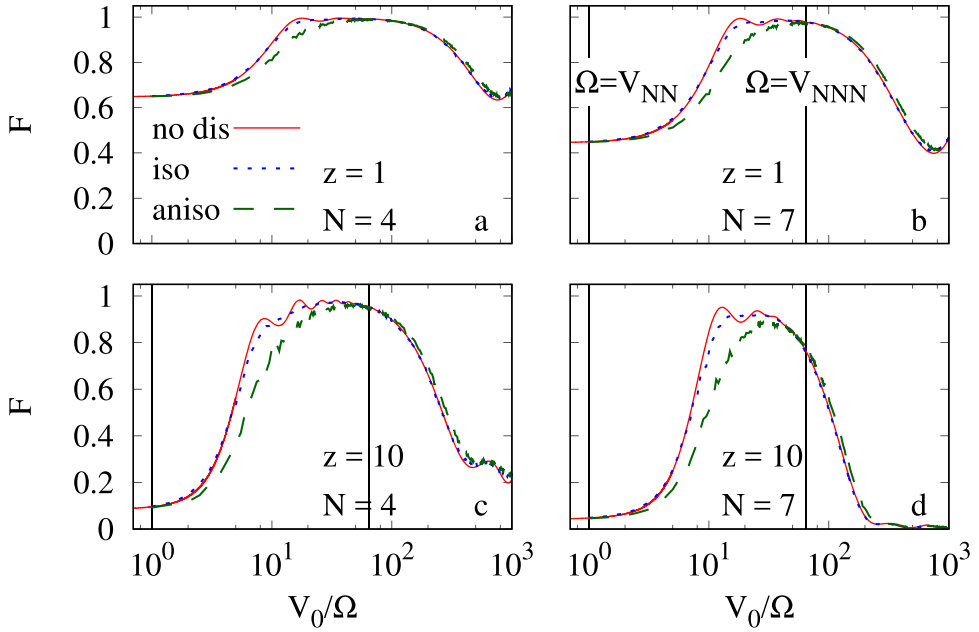

Figure 7. Fidelity of the dimer-MPS preparation protocol as a function of V_0/Ω including the effect of a non-perfect Rydberg blockade and disorder for $N = 4$ (a), (c), $N = 7$ (b), (d) atoms and $z = 1$ (a), (b) and $z = 10$ (c), (d). The solid red, dotted blue and dashed green lines correspond to no, isotropic and anisotropic disorder respectively. Here, F is obtained for 100 realizations of the disorder.

Taking for our comparison parameters from recent experiments [37], in the following we set the trap separation to $r_0 = 4.1\ \mu$m and consider two scenarios for the disorder, one with isotropic disorder ($\sigma_i = 120$ nm, $i = 1, 2, 3$) and one with anisotropic disorder ($\sigma_1 = 1\ \mu$m and $\sigma_{2,3} = 120$ nm). The results presented below are obtained by averaging over 1000 realizations of the disorder unless stated otherwise.

In figures 6–8 we show the fidelity for the GHZ, dimer-MPS and state transport protocols respectively (we take the initial state $|\psi_1\rangle = 1/\sqrt{2}\,(|0\rangle + |1\rangle)$ in the transport protocol). In all plots we compare lines corresponding to a non-perfect blockade and three different choices of disorder: absent (red), isotropic (dotted blue) and anisotropic (dashed green).

The common feature to all plots is that, for the parameters considered, in the large V_0/Ω limit, the blockade mechanism dominates and is only weakly affected by the disorder: here, all three lines show only small differences and sit well on top of each other. Conversely, in the limit of $V_0/\Omega \sim O(1)$, which is of interest for fast application of the protocols such that it still yields high-fidelity outputs (the larger the Ω, the shorter the time needed to apply a pulse of a given area), the disorder has a much stronger impact and in general decreases the fidelity significantly. In that regime, the decrease of fidelity is more pronounced with increasing disorder (situation in all figures 6–8) and also with increasing atom number (compare figures 6(a) and (b), figures 7(a), (c) and (b), (d) and all the panels in figure 8). The decrease of fidelity with the atom number stems from the fact that all our procedures address the atoms sequentially, and therefore each pulse, under imperfect conditions, will make the state diverge more from the target state. In the case of the dimer-MPS protocol, we note that the fidelity

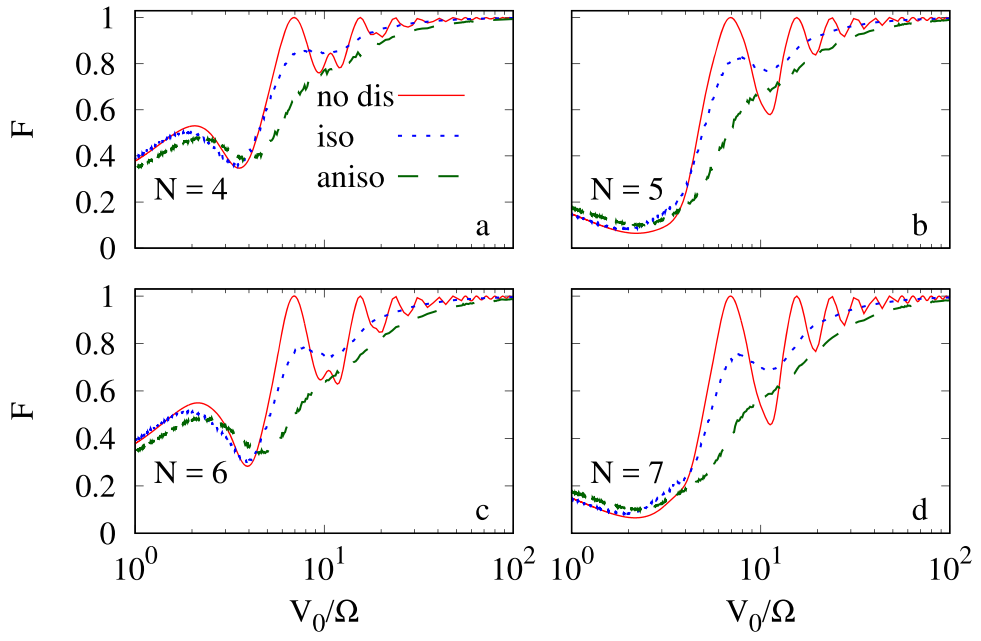

Figure 8. Fidelity of the state transport protocol as a function of V_0/Ω for the initial state $|\psi_1\rangle = 1/\sqrt{2}\,(|0\rangle + |1\rangle)$ and for $N = 4$ (a), $N = 5$ (b), $N = 6$ (c), and $N = 7$ (d). The solid red, dotted blue and dashed green lines correspond to no, isotropic and anisotropic disorder respectively.

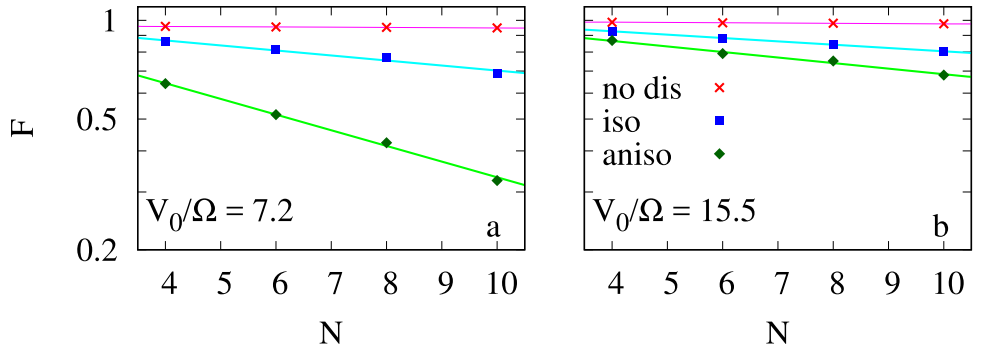

Figure 9. Fidelity of the GHZ protocol as a function of the number of atoms in the chain N for $V_0/\Omega = 7.2$ (a) and $V_0/\Omega = 15.5$ (b). The red crosses, blue squares and green diamonds correspond to no, isotropic and anisotropic disorder respectively. The solid lines represent an exponential function fitted to the data points, see text for details. Data obtained by averaging over 100 realizations of the disorder.

decreases also with increasing z which can be easily understood as higher z correspond to larger number of excitations in the state, which in turn is more sensitive to the disorder.

The main message to be extracted from these results is that all the considered protocols are becoming more sensitive to the positional disorder when approaching the fast operation regime $V_0/\Omega \sim O(1)$ from the large V_0/Ω side, where they are essentially insensitive to the amount of the disorder considered.

In order to further quantify the sensitivity to the disorder and the corresponding decrease in fidelity, we study the fidelity as a function of the length of the chain for the GHZ, dimer-MPS state preparation and state transport protocols, which is shown in figures 9–11 respectively. Here we consider a system with non-perfect Rydberg blockade without disorder (red crosses), with isotropic (blue squares), and anisotropic (green diamonds) disorder. As we are interested in the fast application of the protocols, we have fixed the ratio V_0/Ω to 7.2 and 15.5 in figures 9(a), (b) and to V_0/Ω to 6.9 and 15.5 in figures 11(a), (b) corresponding to the leftmost (second leftmost) peak in the fidelity, see figures 3 and 5 (the optimal values of V_0/Ω used can be extracted numerically or using (27) and (29) respectively). The solid lines correspond to an exponential function $f(N) = a\exp(-b(N-2))$ fitted to the respective data points. Since we consider chains of length $N \geqslant 2$ we set the exponent of the function $f(N)$ to $-b(N-2)$ rather than $-bN$. With such choice of the fitting function, the parameter a in table 2 states the maximal fidelity of the protocol achievable in the simpliest possible system

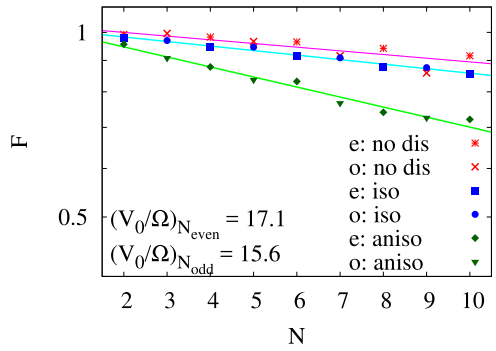

Figure 10. Fidelity of the dimer-MPS protocol as a function of the number of atoms in the chain N for $V_0/\Omega = 17.1$ for even (e) and $V_0/\Omega = 15.6$ for odd (o) number of atoms in the chain and $z = 10$. The red crosses, blue squares and green diamonds correspond to no, isotropic and anisotropic disorder respectively. The solid lines represent an exponential function fitted to the data points, see text for details. Data obtained by averaging over 100 realizations of the disorder.

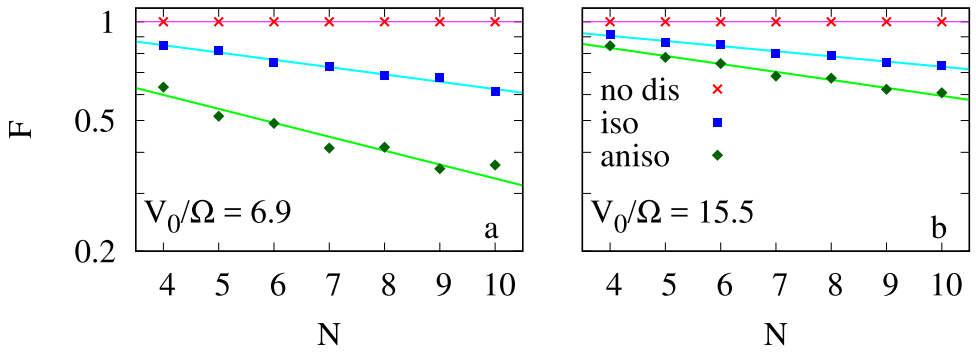

Figure 11. Fidelity of the state transport protocol as a function of the number of atoms in the chain N for $V_0/\Omega = 6.9$ (a) and $V_0/\Omega = 15.5$ (b). The red crosses, blue squares and green diamonds correspond to no, isotropic and anisotropic disorder respectively. The solid lines represent an exponential function fitted to the data points, see text for details. Data obtained by averaging over 1000 realizations of the disorder.

$N = 2$ for different types of disorder. Table 2 shows that the protocols do not reach a fidelity of one when disorder is considered. Figures 9 and 11 further quantify the above discussed observation that the resulting performance is a tradeoff between how fast the protocol can be applied and the resulting fidelity. Interestingly, in the absence of disorder and for V_0/Ω corresponding to the optimal fidelity regions, the final fidelity of the protocols is essentially insensitive to the exact atom number, i.e. is not affected by the tails of the interaction potential, see also figures 3, 5.

Concerning the dimer-MPS state preparation protocol, in order to emphasize the effect of the long-range nature of the interactions on the resulting fidelity, we consider a dimer-MPS state with $z = 10$, corresponding to the largest value we have considered here for this parameter. Our choice of V_0/Ω—corresponding to the two leftmost peaks of the fidelity—for the GHZ preparation and state transport protocols was motivated by the fact that in the absence of disorder these values of V_0/Ω provide a satisfactory tradeoff between the achievable fidelity and the speed of operation independently of the atom number. On the other hand, for the dimer-MPS protocol it is clear from figure 4 ($z = 10$) that a value of V_0/Ω corresponding to the leftmost peak of the $N = 2$ curve yields a rather rapid drop in the fidelity for higher N even in the absence of the disorder. For this reason we consider only the values of V_0/Ω corresponding to the second leftmost peak of the fidelity in figure 4. Here we note that the corresponding value of V_0/Ω slightly varies for odd and even N unlike for the GHZ state preparation and transport protocols. Specifically, we find that $V_0/\Omega \approx 15.6$ and $V_0/\Omega \approx 17.1$ for odd and even N which we use in figure 10.

3.3. Limitations due to spontaneous decay

In sections 3.1, 3.2 we have considered two sources of imperfections introducing errors in the state preparation and state transport protocols, namely the effect of the finiteness of the interaction potential resulting in non-

Table 2. The coefficients of the function $f(N) = a\exp(-b\,(N-2))$ fitted to the data points in figures 9–11 for the GHZ, dimer-MPS state preparation and state transport protocols respectively. The abbreviations correspond to 'no dis' = no disorder, 'iso' = isotropic disorder, 'aniso' = anisotropic disorder parameterized according to the values reported in the main text.

GHZ state				
	$\frac{V_0}{\Omega}=6.9$		$\frac{V_0}{\Omega}=15.5$	
	a	b	a	b
No dis	$0.961015 \pm 6 \times 10^{-6}$	$(1739 \pm 1) \times 10^{-6}$	$0.990331 \pm 7 \times 10^{-6}$	$(1911 \pm 1) \times 10^{-6}$
Iso	0.93 ± 0.02	0.035 ± 0.004	0.970 ± 0.003	0.0234 ± 0.0006
Aniso	0.80 ± 0.01	0.110 ± 0.004	0.94 ± 0.01	0.039 ± 0.003
Dimer-MPS state				
	$\left(\frac{V_0}{\Omega}\right)_{N\ \mathrm{odd}}=15.6$ and $\left(\frac{V_0}{\Omega}\right)_{N\ \mathrm{even}}=17.1$			
	a	b		
No dis	$1.00 - 0.02$	0.0139 ± 0.004		
Iso	0.983 ± 0.004	0.0170 ± 0.0009		
Aniso	0.947 ± 0.009	0.037 ± 0.002		
State transport				
	$\frac{V_0}{\Omega}=6.9$		$\frac{V_0}{\Omega}=15.5$	
	a	b	a	b
No dis	$0.999988 \pm 4 \times 10^{-6}$	$(7.6 \pm 0.8) \times 10^{-7}$	$0.999989 \pm 4 \times 10^{-6}$	$(6.8 \pm 0.8) \times 10^{-7}$
Iso	0.94 ± 0.05	0.051 ± 0.003	0.97 ± 0.01	0.036 ± 0.002
Aniso	0.73 ± 0.04	0.09 ± 0.01	0.93 ± 0.02	0.055 ± 0.003

perfect blockade and the effect of positional disorder of the atoms. We have neglected other noise sources such as spontaneous decay of the atoms from the Rydberg state or loss and dephasing mechanisms due to the interaction of the lattice atoms with the background gas. The reason for this is that we are interested in the short-time dynamics, where these effects become essentially negligible. To give a specific example of a constraint such considerations impose on the evolution of the system, we consider here the example of spontaneous decay.

Motivated by [37], we set the total duration of the experiment to $\tau_{\mathrm{exp}} = 2\ \mu$s, which was used in [37] in order to avoid effects due to the spontaneous photon emission, atom loss and mechanical effects induced by the forces between atoms. As we are considering non-adiabatic state-preparation protocols, we want to find a parameter regime where the protocol can be performed as fast as possible with a high fidelity. Thus, we choose $(V_0/\Omega)^* = 6.9$, corresponding to the position of the leftmost maximum fidelity peak in each protocol (figures 3–5). Finally, we fix $V_0 = 2\pi \times 8.4$ MHz [37]. We can now estimate, with the help of the table 1 and the relations (17), the maximal number of atoms N_{max} so that the total duration of each protocol is smaller than τ_{exp}. The result can be summarized as

$$N_{\mathrm{max}} = (\mathrm{GHZ} \rightarrow 9;\ \mathrm{MPS}(z=1) \rightarrow 13,\ \mathrm{MPS}(z=10) \rightarrow 7;\ \mathrm{transport} \rightarrow 6). \tag{31}$$

One can see, that in this specific $\tau_{\mathrm{exp}} = 2\ \mu$s example, the protocols are limited to rather small number of atoms of the order of 10. In the case of the two-level scheme, where the final state contains Rydberg excitations, the coherence time of the system is dominated by the lifetime τ_l of a single Rydberg atom divided by the number of atoms τ_l/N. At the same time, Rydberg atoms provide multiple possibilities with relaxation timescales ranging over several orders of magnitude, typically from μs to ms regime [3, 41] depending on the Rydberg state. It would thus be interesting to identify the transitions with sufficiently large interaction strength V_0 and long relaxation times. That allows significantly higher N_{max}, which can be in principle achieved by analyzing higher principal quantum number n states (we recall that the interaction strength and relaxation timescales obey approximately the scaling relations $V_0 \propto n^{11}$, $\tau \propto n^3$ [42], while $n = 56$ was used in [37] in the repulsive interaction regime). However, when the three level scheme is used, where the excited Rydberg states are transferred to an atomic hyperfine ground state $|\tilde{1}\rangle$, the coherence time can be seen to last up to several tens of seconds as outlined in [43].

4. Conclusions

We have described three different protocols for QIP based on non-adiabatic manipulation of atoms. The protocols exploit the Rydberg blockade mechanism and require single site addressability, which is now an available experimental tool. Specifically, we have shown how to generate antiferromagnetic GHZ states, a class of MPSs—the dimer-MPS—which include the Rydberg crystals, and quantum state transport in chains of Rydberg atoms. We have evaluated the effect of the full interaction potential on the quality of the protocols identifying a parameter regime yielding optimal performance in terms of fast operation resulting in output states with high fidelity. Next, we have evaluated the experimentally relevant effect of positional disorder stemming from the finite temperature of the atoms and width of the optical traps respectively, and quantified its influence on the fidelity. Finally, we have discussed the constraints imposed on the presented protocols by other sources of imperfections, namely the relaxation of the Rydberg states.

Acknowledgments

We would like to thank Daniel Barredo, Antoine Browaeys, Thierry Lahaye, Sylvain de Léséleuc and Markus Müller for fruitful discussions. The research leading to these results has received funding from the European Research Council under the European Union's Seventh Framework Programme (FP/2007-2013) / ERC Grant Agreement No. 335266 (ESCQUMA), the EU-FET Grant No. 512862 (HAIRS), the H2020-FETPROACT-2014 Grant No. 640378 (RYSQ), and EPSRC Grant No. EP/M014266/1.

Appendix A. Toffoli gate

The basic building block of the protocols studied in this work is the three-body Hamiltonian (3) and the associated unitary gate (4). The latter provides a tool to implement various three-body gates, where the specific properties of the gate are determined by the parameters of the Hamiltonian, namely the detuning Δ_k, Rabi frequency Ω_k and the duration of the pulse t_k on kth atom. In the specific case, where $\Delta_k = 0$ for all atoms and the area of the pulse applied at the kth atom $\Omega_k t_k = \pi$, the unitary (4) corresponds to the Toffoli gate.

Here, in table A1, we list for completeness the properties of the Toffoli gate used in the quantum state transport protocol. The first and last qubits are the control ones while the second qubit is the target. Provided that both control qubits are in state $|0\rangle$ the Toffoli gate acts like a π-pulse on the target qubit.

Table A1. Truth table of the Toffoli gate. The first and the third qubits are the control qubits, while the second qubit is the target. When the control qubits are both in the ground state $|0\rangle$, the Toffoli gate corresponds to an application of a π-pulse on the target qubit.

Input	Output
000	010
001	001
010	000
011	011
100	100
101	101
110	110
111	111

Appendix B. On the derivation of the effective Hamiltonian

To the lowest order in the perturbation, the effective Hamiltonian is obtained by applying the unitary transformation $\hat{U} = \exp(\mathrm{i}\, t\ V \sum_k^N \hat{n}_k\ \hat{n}_{k+1})$ on (1). Using the rotating wave approximation, this leads to

$$\hat{H}_{\rm int} = \Omega \sum_{k=1}^{N} \hat{\sigma}_y^k \, (1 - \hat{n}_{k-1})(1 - \hat{n}_{k+1}) + \frac{V_0}{64} \sum_{k=1}^{N} \hat{n}_k \, \hat{n}_{k+2}. \tag{B1}$$

Next, the second term in (B1) is suppressed by a factor 64 and is neglected, which yields the effective Hamiltonian (3).

Appendix C. Dimer-MPS

C.1. Derivation of the recurrence formulae

We discuss here how to retrieve a recursion formula for the areas A_k in the case where an excitation blocks its first R neighbors to the right and to the left. Formula (16) will correspond to the particular case $R = 1$. We start by recalling that the target state is expressed as

$$|z\rangle = \frac{1}{\sqrt{Z_z}} \prod_{k=1}^{L} (\mathbb{1} + z \, \hat{P}_{k,\rm left} \, \hat{\sigma}_k^+ \, \hat{P}_{k,\rm right}) | \downarrow \ldots \downarrow \rangle, \tag{C1}$$

where $\hat{P}_{k,\rm left} = \hat{P}_{k-1} \ldots \hat{P}_{k-R}$ and $\hat{P}_{k,\rm right} = \hat{P}_{k+1} \ldots \hat{P}_{k+R}$. The action of a local pulse on the kth atom depends on whether the latter is blockaded (i.e. there are excitations within a radius R) or not. In the former case, we have

$$\hat{U}_k^{01}(A_k)|0_k\rangle = |0_k\rangle. \tag{C2}$$

Conversely, if the atom is not blockaded,

$$\hat{U}_k^{01}|0_k\rangle(A_k) = \cos A_k |0_k\rangle + \sin A_k |1_k\rangle. \tag{C3}$$

We now think of applying an ordered sequence of these unitary operations addressing one atom at a time, from the first to the last $\hat{U} = \prod_{k=N}^{1} \hat{U}_k^{01}$, to a ground-state configuration $|0_1 \ldots 0_N\rangle$. This will yield a state with components on all configurations in which no pairs of excitations appear at a distance $\leqslant R$. Note that, according to (C3), the ground state configuration will come with a coefficient

$$C_0 \equiv \prod_{k=N}^{1} \cos A_k. \tag{C4}$$

Every configuration with an excitation in site j will instead feature a factor $\sin A_j$. Furthermore, because of the blockade, the operations acting on $j = k + 1, \ldots, k + R$ will behave as displayed in (C2), i.e. they will trivially contribute 1 to the overall coefficient. In general, we can reconstruct the coefficient of a generic configuration via the following simple rules:

(i) Choose a configuration and start reading it from the first atom to be addressed to the last one. Assign a coefficient 1 to start with.

(ii) Until a $|1\rangle$ is found, for every $|0_k\rangle$ multiply the coefficient by $\cos A_k$.

(iii) When a $|1_k\rangle$ is found, multiply by $\sin A_k$ and skip to position $k + R + 1$.

(iv) Apply (ii) again.

Hence, if we call $C_j^{(1)}$ the coefficient of the configuration with a single excitation in site j we have

$$\frac{C_j^{(1)}}{C_0} = \frac{\sin A_j}{\prod_{k=j}^{j+R} \cos A_k}. \tag{C5}$$

More in general, the coefficient $C^{(\vec{n})}$ of an allowed state with n excitations in positions $\vec{n} = \{j_1, \ldots j_n\}$ will obey

$$\frac{C^{(\vec{n})}}{C_0} = \prod_{\mu=1}^{n} \frac{\sin A_{j_\mu}}{\prod_{k=j_\mu}^{j_\mu+R} \cos A_k}. \tag{C6}$$

The correct form of state $|z\rangle$ is then reproduced by fixing the areas in such a way that

$$\frac{\sin A_j}{\prod_{k=j}^{j+R} \cos A_k} = z \quad \forall \; z. \tag{C7}$$

This defines a recursion for A_j in terms of $A_{j+1}, \ldots, A_{j+R}$. In order to make the solution of the recursion unique, we need to also impose the boundary conditions

$$\cos A_{N+j} = 1 \quad \forall \quad 1 \leqslant j \leqslant R. \tag{C8}$$

Note that the recursion relation can be also cast in the form

$$\tan A_j = z \prod_{k=j+1}^{j+R} \cos A_k. \tag{C9}$$

Since the tan function is π-periodic, we have the freedom to choose the sign of the cosines, which we determine to be all positive. This means that the sign of the sines will instead coincide with the sign of the parameter z. This uniquely identifies the areas A_k modulo 2π.

C.1.1. Nearest-neighbor case. Here, we solve the recursion relation (16) in the simplest case $R = 1$. By defining

$$x_k = \cos^2 A_{L+1-k} \tag{C10}$$

and $a = z^2$ we find

$$x_{k+1} = \frac{1}{1 + a\, x_k} \tag{C11}$$

with seed $x_0 = 1$. We now rewrite $x_k = p_k/q_k$, which yields

$$\frac{p_{k+1}}{q_{k+1}} = \frac{q_k}{q_k + a\, p_k} \tag{C12}$$

and assume that we can separate numerator and denominator as if they were independent, leading to the system

$$p_{k+1} = q_k, \tag{C13}$$

$$q_{k+1} = q_k + a\, q_{k-1}. \tag{C14}$$

In order to correctly reproduce the boundary condition for x_k, we ask $q_0 = q_{-1} = p_0 = 1$. Since $a \geqslant 0$, we see that if $q_k > 0$ and $q_{k-1} > 0$, then $q_{k+1} > 0$ as well. Given the initial conditions, it follows from induction that $q_k > 0\ \forall\, k$. Furthermore,

$$q_{k+1} \geqslant q_k = p_{k+1}, \tag{C15}$$

as expected since by definition $x_k = p_k/q_k = q_{k-1}/q_k$ must be $\leqslant 1$.

The recursion equation for q_k is linear and can be solved exactly: the associated polynomial is $\lambda^2 - \lambda - a$, whose roots are

$$\lambda_\pm = \frac{1 \pm \sqrt{1 + 4a}}{2}. \tag{C16}$$

Therefore, the general solution is

$$q_k = A\lambda_+^k + B\lambda_-^k, \tag{C17}$$

with A and B fixed via the boundary conditions $q_{-1} = q_0 = 1$, which yield

$$A = \frac{1 + 2a + \sqrt{1 + 4a}}{2\sqrt{1 + 4a}} = \frac{1}{\sqrt{1 + 4a}}\left(\frac{1 + \sqrt{1 + 4a}}{2}\right)^2$$
$$B = \frac{-1 - 2a + \sqrt{1 + 4a}}{2\sqrt{1 + 4a}} = -\frac{1}{\sqrt{1 + 4a}}\left(\frac{1 - \sqrt{1 + 4a}}{2}\right)^2.$$

Thereby, we find

$$q_k = \frac{1}{\sqrt{1 + 4a}}\left[\left(\frac{1 + \sqrt{1 + 4a}}{2}\right)^{k+2} - \left(\frac{1 - \sqrt{1 + 4a}}{2}\right)^{k+2}\right] \tag{C18}$$

and, consequently,

$$x_k = \frac{p_k}{q_k} = \frac{\left(\frac{1+\sqrt{1+4a}}{2}\right)^{k+1} - \left(\frac{1-\sqrt{1+4a}}{2}\right)^{k+1}}{\left(t\frac{1+\sqrt{1+4a}}{2}\right)^{k+2} - \left(\frac{1-\sqrt{1+4a}}{2}\right)^{k+2}}$$
$$= 2\frac{(1 + \sqrt{1 + 4a})^{k+1} - (1 - \sqrt{1 + 4a})^{k+1}}{(1 + \sqrt{1 + 4a})^{k+2} - (1 - \sqrt{1 + 4a})^{k+2}}, \tag{C19}$$

which exactly corresponds to equation (18), since we have chosen the cosines to be positive.

C.1.2. Generic R case. The general case is defined by

$$x_{k+1} = \frac{1}{1 + a\prod_{j=k}^{k+1-R} x_j}. \tag{C20}$$

The same trick as above $x_k = p_k/q_k$ can be applied, yielding

$$\frac{p_{k+1}}{q_{k+1}} = \frac{\prod_{j=k}^{k+1-R} q_j}{\prod_{j=k}^{k+1-R} q_j + a\prod_{j=k}^{k+1-R} p_j}. \tag{C21}$$

The same choice $p_k = q_{k-1}$ gives now

$$q_{k+1} = q_k + aq_{k-R}, \tag{C22}$$

which is associated to the polynomial

$$\lambda^{R+1} = \lambda^R + a, \tag{C23}$$

which is generally not analytically solvable. However, it has $R + 1$ (complex) roots λ_j and the general implicit solution of the recursion is

$$q_k = \sum_{j=1}^{R+1} A_j \lambda_j^k. \tag{C24}$$

Imposing the boundary conditions yields a system of equations for the coefficients A_j with equations of the form

$$\sum_{j=1}^{R+1} \frac{A_j}{\lambda_j^n} = 1, \tag{C25}$$

for $n = -R,\ldots,0$ which can be also written as

$$\sum_{j=1}^{R+1} M_{nj} A_j = 1 \quad \forall\ n, \tag{C26}$$

where M_{nj} is a matrix with entries $M_{nj} = \lambda_j^n$, i.e. it is a Vandermonde matrix. By using Cramer's rule for the solution of linear systems of equations, we can write the coefficient A_k as

$$A_k = \frac{\det M^{(k)}}{\det M}, \tag{C27}$$

where $M^{(k)}$ is constructed from M by substituting 1 to all entries on the kth column. Note that $M^{(k)} = M$ if $\lambda_k = 1$, which means that $M^{(k)}$ is also a Vandermonde matrix. Exploiting the known structure of the determinants of Vandermonde matrices we can thus write

$$A_k = \frac{\prod_{1\leqslant i<j\leqslant R+1} \left(\frac{1}{\lambda_j^{(k)}} - \frac{1}{\lambda_i^{(k)}}\right)}{\prod_{1\leqslant i<j\leqslant R+1} \left(\frac{1}{\lambda_j} - \frac{1}{\lambda_i}\right)}, \tag{C28}$$

where $\lambda_j^{(k)} = \lambda_j$ if $j \neq k$ and 1 otherwise. By simplifying all common factors, this can also be rewritten as

$$A_k = \lambda_k^R \frac{\prod_{j\neq k} (1 - \lambda_j)}{\prod_{j\neq k} (\lambda_k - \lambda_j)}. \tag{C29}$$

C.2. Comment on the dimer-MPS as a ground state of the Rydberg Hamiltonian

In [27] it has been demonstrated that, in a specific regime of the parameters, the Hamiltonian (1) can be approximately mapped to a Rokhsar–Kivelson form [30], which is associated with the stochastic matrix describing the evolution of a classical stochastic process [44]. These Hamiltonians admit an exact solution for their ground states. In particular, as shown in [27], Hamiltonian (1) admits such a representation when its parameters satisfy $\Omega_k = \Omega$, $\forall\, k$, and

$$\Delta_k \equiv \Delta = 2^6 \frac{\Omega^2}{V_0} - \frac{3V_0}{2^6}, \tag{C30}$$

which identifies a manifold in the parameter space. Under these conditions, and assuming that interactions among nearest neighbors are strong enough to enforce an almost perfect blockade, while becoming sufficiently small beyond next-nearest neighbors to be safely neglected, the ground state of the system is well approximated by (9), where $z = -V_0/(2^6\Omega)$.

Next, as mentioned in the main text, the same construction can be extended to the case of the blockade effect extending beyond nearest neighbors: assuming that an excitation prevents its first R neighbors from being excited, the many-body ground state can be again analytically expressed in the parameter manifold [29] as

$$\Delta = \frac{\Omega^2}{V_R} - V_R\,(2\,R + 1), \tag{C31}$$

where $V_R = C_6/(r_0^6(R+1)^6)$, and takes the generalized form (11).

References

[1] Bloch I, Dalibard J and Zwerger W 2008 Many-body physics with ultracold gases *Rev. Mod. Phys.* **80** 885–964
[2] Bloch I, Dalibard J and Nascimbene S 2012 Quantum simulations with ultracold quantum gases *Nat. Phys.* **8** 267–76
[3] Saffman M, Walker T G and Mølmer K 2010 Quantum information with Rydberg atoms *Rev. Mod. Phys.* **82** 2313
[4] Weimer H, Müller M, Lesanovsky I, Zoller P and Büchler H P 2010 A Rydberg quantum simulator *Nat. Phys.* **6** 382–8
[5] Saffman M 2016 Quantum computing with atomic qubits and Rydberg interactions: progress and challenges *J. Phys. B: At. Mol. Opt. Phys.* **49** 202001
[6] Labuhn H, Barredo D, Ravets S, de Léséleuc S, Macrì T, Lahaye T and Browaeys A 2016 Tunable two-dimensional arrays of single Rydberg atoms for realizing quantum ising models *Nature* **534** 667
[7] Schauß P, Zeiher J, Fukuhara T, Hild S, Cheneau M, Macrì T, Pohl T, Bloch I and Groß C 2015 Crystallization in Ising quantum magnets *Science* **347** 1455–8
[8] Jau Y-Y, Hankin A M, Keating T, Deutsch I H and Biedermann G W 2016 Entangling atomic spins with a Rydberg-dressed spin-flip blockade *Nat. Phys.* **12** 71–4
[9] Isenhower L, Urban E, Zhang X L, Gill A T, Henage T, Johnson T A, Walker T G and Saffman M 2010 Demonstration of a neutral atom controlled-not quantum gate *Phys. Rev. Lett.* **104** 010503
[10] Maller K M, Lichtman M T, Xia T, Sun Y, Piotrowicz M J, Carr A W, Isenhower L and Saffman M 2015 Rydberg-blockade controlled-not gate and entanglement in a two-dimensional array of neutral-atom qubits *Phys. Rev.* A **92** 022336
[11] Nogrette F, Labuhn H, Ravets S, Barredo D, Béguin L, Vernier A, Lahaye T and Browaeys A 2014 Single-atom trapping in holographic 2d arrays of microtraps with arbitrary geometries *Phys. Rev.* X **4** 021034
[12] Barredo D, de Léséleuc S, Lienhard V, Lahaye T and Browaeys A 2016 An atom-by-atom assembler of defect-free arbitrary two-dimensional atomic arrays *Science* **354** 1021–3
[13] Endres M, Bernien H, Keesling A, Levine H, Anschuetz E R, Krajenbrink A, Senko C, Vuletic V, Greiner M and Lukin M D 2016 Atom-by-atom assembly of defect-free one-dimensional cold atom arrays *Science* **354** 1024–7
[14] Labuhn H, Ravets S, Barredo D, Béguin L, Nogrette F, Lahaye T and Browaeys A 2014 Single-atom addressing in microtraps for quantum-state engineering using Rydberg atoms *Phys. Rev.* A **90** 023415
[15] Boll M, Hilker T A, Guillaume S, Omran A, Nespolo J, Pollet L, Bloch I and Gross C 2016 Spin-and density-resolved microscopy of antiferromagnetic correlations in Fermi–Hubbard chains *Science* **353** 1257–60
[16] Bakr W S, Gillen J I, Peng A, Fölling S and Greiner M 2008 A quantum gas microscope for detecting single atoms in a Hubbard-regime optical lattice *Nature* **462** 74–8
[17] Cheuk L W, Nichols M A, Okan M, Gersdorf T, Ramasesh V V, Bakr W S, Lompe T and Zwierlein M W 2015 Quantum-gas microscopy for fermionic atoms *Phys. Rev. Lett.* **114** 193001
[18] Petrosyan D, Mølmer K and Fleischhauer M 2016 On the adiabatic preparation of spatially-ordered Rydberg excitations of atoms on a one-dimensional optical lattice by laser frequency sweeps *J. Phys. B: At. Mol. Opt. Phys.* **49** 084003
[19] Cui J, van Bijen R, Pohl T, Montangero S and Thomas C 2017 Optimal control of Rydberg lattice gases *Quantum Science Technol.* **2** 035006
[20] Giovannetti V, Lloyd S and Maccone L 2004 Quantum-enhanced measuements: beating the standard quantum limit *Science* **306** 1330
[21] Mølmer K and Sørensen A 1999 Multiparticle entanglement of hot trapped ions *Phys. Rev. Lett* **82** 1835
[22] Wang D-W 2016 Sewing Greenberg–Horne–Zeilinger states with a quantum zipper arXiv:1609.08589
[23] Monz T, Schindler P, Barreiro J T, Chwalla M, Nigg D, Coish W A, Harlander M, Hänsel W, Hennrich M and Blatt R 2011 14-Qubit Entanglement: creation and Coherence *Phys. Rev. Lett.* **106** 130506
[24] Schollwöck U 2005 The density-matrix renormalization group *Rev. Mod. Phys.* **77** 259–315
[25] Perez-Garcia D, Verstraete F, Wolf M M and Cirac J I 2007 Matrix product state representations *Quantum Inf. Comput.* **7** 401
[26] Schollwöck U 2011 The density-matrix renormalization group in the age of matrix product states *Ann. Phys., NY* **326** 96–192
[27] Lesanovsky I 2011 Many-Body spin interactions and ground state of a dense Rydberg lattice gas *Phys. Rev. Lett.* **106** 025301
[28] Lesanovsky I 2012 Liquid ground state, gap and excited states of a strongly correlated spin chain *Phys. Rev. Lett.* **108** 105301
[29] Levi E and Lesanovsky I 2014 Non-classical correlations in a class of spin chains with long-range interactions and exactly solvable ground states *New J. Phys.* **16** 093053
[30] Rokhsar D S and Kievelson S A 1988 Superconductivity and the quantum hard-core dimer gas *Phys. Rev. Lett* **61** 2376
[31] Schachenmayer J, Lesanovsky I, Micheli A and Daley A J 2010 Dynamical crystal creation with polar molecules or Rydberg atoms in optical lattices *New J. Phys.* **12** 103044
[32] Van Bijnen R M W, Smit S, Van Leeuwen K A H, Vredenbregt E J D and Kokkelmans S J J M F 2011 Adiabatic formation of Rydberg crystals with chirped laser pulses *J. Phys. B: At. Mol. Opt. Phys.* **44** 184008
[33] Pohl T, Demler E and Lukin M D 2010 Dynamical crystallization in the dipole blockade of ultracold atoms *Phys. Rev. Lett.* **104** 043002
[34] Bennett C H and DiVincenzo D P 2000 Quantum information and computation *Nature* **404** 247
[35] Cirac J I, Zoller P, Kimble H J and Mabuchi H 1997 Quantum state transfer and entanglement distribution amond distant nodes in a quantm network *Phys. Rev. Lett.* **78** 3221
[36] Saffman M and Walker T G 2005 Entangling single- and N-atom qubits for fast quantum state detection and transmission *Phys. Rev.* A **72** 042302
[37] Marcuzzi M, Jiří M, Barredo D, de Léséleuc S, Labuhn H, Lahaye T, Browaeys A, Levi E and Lesanovsky I 2017 Facilitation dynamics and localization phenomena in Rydberg lattice gases with position disorder *Phys. Rev. Lett.* **118** 063606
[38] Thaicharoen N, Schwarzkopf A and Raithel G 2015 Measurement of the van der waals interaction by atom trajectory imaging *Phys. Rev.* A **92** 040701

[39] Faoro R, Simonelli C, Archimi M, Masella G, Valado M M, Arimondo E, Mannella R, Ciampini D and Morsch O 2016 van der waals explosion of cold Rydberg clusters *Phys. Rev.* A **93** 030701
[40] Bennet C H, Brassard G, Crépeau C, Josza R, Peres A and Wootters W K 1993 Teleporting an unkown quantum state via dual classical and Einstein–Podolsky–Rosen channels *Phys. Rev. Lett.* **70** 1895
[41] Gallagher T F (ed) 1994 *Rydberg atoms* (Cambridge: Cambridge University Press)
[42] Löw R, Weimer H, Nipper J, Balewski J B, Butscher B, Büchler H P and Pfau T 2012 An experimental and theoretical guide to strongly interacting Rydberg gases *J. Phys. B: At. Mol. Opt. Phys.* **45** 113001
[43] Szmuk R, Dugrain V, Maineult W, Reichelt J and Rosenbusch P 2015 Stability of a trapped-atom clock on a chip *Phys. Rev.* A **92** 012106
[44] Castelnovo C, Chamon C, Mudry C and Pujol P 2005 From quantum mechanics to classical statistical physics: generalized Rokhsar Kivelson hamiltonians and the stochastic matrix form decomposition *Ann. Phys., NY* **318** 344
[45] Bose S 2003 *Phys. Rev. Lett.* **91** 207901
[46] Bose S 2007 *Contemp. Phys.* **48** 13–30
[47] Burgarth D and Bose S 2005 *New J. Phys.* **7** 135